

This item is the archived peer-reviewed author-version of:

Homogeneous flow and size dependent mechanical behavior in highly ductile $Zr_{65}Ni_{35}$ metallic glass films

Reference:

Ghidelli Matteo, Idrissi Hosni, Gravier Sébastien, Blandin Jean-Jacques, Raskin Jean-Pierre, Schryvers Dominique, Pardoën Thomas.- Homogeneous flow and size dependent mechanical behavior in highly ductile $Zr_{65}Ni_{35}$ metallic glass films

Acta materialia - ISSN 1359-6454 - 131(2017), p. 246-259

Full text (Publisher's DOI): <https://doi.org/10.1016/J.ACTAMAT.2017.03.072>

To cite this reference: <https://hdl.handle.net/10067/1426420151162165141>

**Homogeneous flow and size dependent mechanical behavior
in highly ductile $Zr_{65}Ni_{35}$ metallic glass films**

Matteo Ghidelli^{1,2,3*}, Hosni Idrissi^{3,4}, Sébastien Gravier¹, Jean-Jacques Blandin¹, Jean-Pierre Raskin²,
Dominique Schryvers⁴, Thomas Pardoen^{3*}

¹ Science and engineering of materials and processes, SIMaP, Université de Grenoble / CNRS, UJF / Grenoble INP, BP46, 38402, Saint-Martin d'Hères, France.

² Institute of information and communication technologies, electronics and applied mathematics, ICTEAM, Université catholique de Louvain, B-1348, Louvain-la-Neuve, Belgium.

³ Institute of mechanics, materials and civil engineering, IMMC, Université catholique de Louvain, B-1348, Louvain-la-Neuve, Belgium.

⁴ EMAT, University of Antwerp, Groenenborgerlaan 171, B-2020 Antwerp, Belgium

*e-mail: matteo.ghidelli@uniroma3.it, thomas.pardoen@uclouvain.be

Abstract

Motivated by recent studies demonstrating a high strength - high ductility potential of nano-scale metallic glass samples, the mechanical response of freestanding $Zr_{65}Ni_{35}$ film with sub-micron thickness has been investigated by combining advanced on-chip tensile testing and electron microscopy. Large deformation up to 15% is found for specimen thicknesses below 500 nm with variations depending on specimen size and frame compliance. The deformation is homogenous until fracture, with no evidence of shear banding. The yield stress is doubled when decreasing the specimen cross-section, reaching ~ 3 GPa for small cross-sections. The fracture strain variation is related to both the stability of the test device and to the specimen size. The study concludes on clear disconnect between the mechanisms controlling the onset of plasticity and the fracture process.

Keywords

Metallic glass; thin films; size effects; mechanical properties; on-chip testing.

1. Introduction

Compared with crystalline metals that show large tensile ductility with significant uniform elongation, bulk metallic glasses (BMGs) are essentially brittle at room temperature [1-3]. Narrow (~ 10 nm-thick) shear bands develop as the stress gets large enough with severe plastic-strain localization leading to catastrophic failure [1-3]. Recent reports have shown that the brittle-like behavior is mitigated when the sample size is reduced down to the sub-micron scale. This mechanical *size effect* has been predicted by molecular dynamic simulations [4, 5] and experimentally demonstrated using compression (or tension) test of micropillars [6-9] or *in-situ* transmission electron microscopy (TEM) tensile tests [8, 10, 11].

Volkert *et al.* [6, 12] reported a transition from shear band mediated plastic flow to homogeneous deformation under compressive loading when the diameter of amorphous $Pd_{77}Si_{23}$ micropillars is below

400-500 nm. Jang and Greer [7] and Chen *et al.* [13] confirmed this trend showing that 100 nm-thick nanopillars deform homogeneously in tension. Other studies [8, 9, 14-17] reported contradicting results with the formation of shear bands even for the smallest pillars. Some authors found an increase of yield strength for decreasing diameter [7, 14, 15], while others did not detect any change or even a small decrease [6, 9, 16-18]. Guo *et al.* [11] deformed Zr-based thin film metallic glasses (TFMGs) in tension inside a TEM, with 100 x 100 x 250 nm sized specimens sustaining plastic deformation up to 45% but without stress measurement. Deng *et al.* [10] and Jiang *et al.* [19] confirmed these results for 50 nm-thick $\text{Cu}_{49}\text{Zr}_{51}$ and $\text{Ni}_{60}\text{Nb}_{40}$ TFMGs reporting a ductility up to 12% and 40%, respectively, but the test was not instrumented for force measurement. Tian *et al.* [20], using dogbone shape specimens, extracted the full stress-strain curve of 200 nm-thick $\text{Cu}_{49}\text{Zr}_{51}$ TFMGs showing large elastic deformation $\sim 4\%$ coupled with a yield strength close to the theoretical value of 3.7 GPa. Lastly, in our recent studies [21, 22], we found size effects on the failure behavior and fracture toughness of submicrometer sized $\text{Zr}_{65}\text{Ni}_{35}$ TFMGs related to geometric confinement and not due to a compositional or structural change as a function of thickness.

A conclusive understanding of the origin of size effects and of the associated mechanisms for the formation or not of catastrophic shear bands is still missing. The difficulty comes from the challenge to generate consistent and reproducible data on extremely small specimens, while avoiding artifacts. In micropillar compression, the sample geometry can have a rounded tip and tapered shape, while imperfect punch-pillar contact leads to stress concentration [8]. Information about the magnitude of the stress in *in-situ* TEM is often missing, while the attainment of large plastic deformation is strongly dependent on the loading set-up, machine stiffness and specimen alignment affecting shear bands stability [2, 10]. Specimens are most often produced by Focus Ion Beam (FIB) involving high energy Ga^+ ions. This operation alters the mechanical behavior by chemical softening and free-volume generation [23, 24].

Lastly, a complete picture of mechanical size effects over a broad range of specimen geometries and sizes is missing, with most reported works involving only a limited number of test specimens.

The objectives of this work are to investigate the behavior of $Zr_{65}Ni_{35}$ (% at.) TFMGs deformed in tension and to analyze the size dependent strength and ductility. More specifically, we report the successful fabrication of freestanding fully amorphous $Zr_{65}Ni_{35}$ metallic glass tensile test specimens avoiding FIB milling, while studying a broad range of geometries to investigate how size affects strength and ductility. This lab-on-chip method [25, 26] allows the testing of a large number of almost perfectly aligned micron and sub-micron sized elementary specimens, around one thousand in this study, each one giving one specific point on the stress-strain curve.

The outline of the paper is the following. The lab-on-chip mechanical testing method is presented in Section 2 providing all the details of the fabrication and the extraction of mechanical properties. Section 3 focuses on the results about mechanical size effects, SEM and high resolution TEM (HRTEM) observations. Lastly, Section 4 is dedicated to the discussion.

2. Experiments

2.1 Lab-on-chip technique for mechanical testing

The on-chip technique based on residual stress actuated microtensile testing structures developed at Université catholique de Louvain (UCL) [25-27] is applied here for the first time to metallic glasses (Fig. 1a,b). A long dogbone test specimen made by metallic glass overlaps a Si_3N_4 actuator beam involving tensile residual stress ~ 1 GPa [28] both patterned by lithography. The “actuator + specimen” constitutes one elementary test structure. Upon release (Fig. 1b), the actuator contracts and pulls on the specimen beam, which is almost perfectly aligned with the loading direction, until force equilibrium is reached [25, 26]. Tests are simultaneously performed on hundreds of specimens with different geometries for the determination of the uniaxial entire stress-strain response up to fracture. We successively present

hereafter (i) the fabrication steps involved in the generation of the test structures, (ii) the data reduction scheme to extract the stress and strain applied to each specimen, and (iii) the mechanical stability analysis for this specific test configuration.

2.1.1 Fabrication of micro-tensile freestanding specimens

A complete description of the generic steps for the production of the on-chip test structures can be found in Refs. [25-27]. Its applications to TFMGs is explained hereafter. Firstly, Si (100) wafer is cleaned with $\text{H}_2\text{SO}_4:\text{H}_2\text{O}_2$ solution followed by a 2% vol. $\text{HF}:\text{H}_2\text{O}$. The actuator layer (Si_3N_4) is deposited by Low Pressure Chemical Vapor Deposition (LPCVD). The difference in thermal expansion coefficient between the thin Si_3N_4 layer and the Si substrate combined with the high deposition temperature (790°C) leads to ~ 1 GPa residual stress in the actuator layer [26-28]. The actuator residual stress (σ_{ra}) has been measured using Stoney equation by evaluating the variation of the radius of curvature of a Si wafer coated with a Si_3N_4 layer, see Ref. [28].

Then, the actuator mismatch strain (ε_a^{mis}) - which is an essential ingredient for the determination of the stress applied to the specimen (see further) - is obtained as $\frac{\sigma_{ra}}{E_a}(1-\nu_a)$ from equibiaxial elastic conditions, where E_a – measured using nanoindentation – is equal to 250 GPa and ν_a has been taken equal to 0.24 [25-28]. In addition, ε_a^{mis} has also been directly estimated from measurements of the contraction of free actuators upon release [27, 28]. For all thicknesses investigated ε_a^{mis} was found equal to -0.003 ± 0.0005 in agreement with earlier results, see Refs. [25-27]. The Si_3N_4 layer is then patterned in the shape of long beams (see Fig. 1a,b) by photolithography and by dry etching (SF_6 plasma). The thickness of the actuator layer is modified for each specific specimen thickness in order to optimize the accuracy of the method (see Ref [26] for details about the error analysis). Here the actuator thicknesses are equal to 80, 100, 160 or 350 nm for specimen thicknesses equal to 110, 200, 360 and 550 nm,

respectively. The length of the actuator beam is varied between 100 and 4000 μm in order to generate different levels of deformation in the test specimens. The actuator beam width is equal to 15 μm . The specimen layer is deposited by DC-magnetron sputtering (details in Refs. [21, 22]). It is patterned using a photolithography lift-off technique.

The specimens have a dog-bone shape as sketched in Figure 1a,b in order to ensure perfect uniaxial tension condition along the entire section and to avoid stress concentration at the edges. A variation of the specimen thickness along the width has been observed on SEM cross-sections, caused by the lift-off process. The impact of this non-uniform thickness on the extracted mechanical properties is discussed in the Appendix. The residual stress in the specimen has been measured using Stoney equation by evaluating the difference of the curvature radius of a Si wafer coated with the $\text{Zr}_{65}\text{Ni}_{35}$ layer [25-27]. Then, the specimen mismatch strain (ε^{mis}) is given by $\frac{\sigma_r}{E}(1-\nu)$ where E and ν have been extracted using Brillouin spectroscopy as equal to 72 GPa and 0.39, respectively (see Ref. [22]). For all thicknesses, ε^{mis} was found equal to $+0.0017 \pm 0.0003$, where the positive sign indicates that the stresses are compressive (i.e. the corresponding residual stress results from an elastic strain that is exactly equal to $-\varepsilon^{mis}$).

The release of the actuator is performed by wet etching the silicon substrate in 10% vol. TMAH (tetramethylammonium hydroxide): H_2O solution at 85°C. Freestanding films have been obtained after 17 minutes immersion, a condition which gives a minimum underetching equal to $\sim 20 \mu\text{m}$. After release, the actuator and the specimen beams are then detached from the substrate and thus free to move. The force relaxes in the actuator beam while it increases in the specimen beam until equilibrium is reached [25-27], see SEM images in Figures 1c,d. The specimen beam elongates and this gives rise to a displacement between the fixed and moving cursors (Fig. 1c). After etching, the samples are left in H_2O

first and then in isopropanol for 50 minutes in order to stop the etching reaction. Critical point drying is then performed in order to avoid stiction of the structures onto the underlying substrate.

All the specimen dimensions are summarized in Table 1: these dimensions are significantly larger than in the works cited earlier [6, 7, 10, 11, 14, 20] covering almost one and even two decades in terms of specimen cross-section area and volume variations, respectively.

2.1.2 Extraction of stress and strain

The stress (σ) and mechanical strain (ε^{mech}) can be directly inferred from the displacement (u) between the moving and fixed cursors and from the mismatch strain of the actuator (ε_a^{mis}) and test specimen (ε^{mis}) (Figure 1c) [25, 26]. The mechanical strain in the specimen and actuator is given, respectively, by

$$\varepsilon^{mech} = \ln\left(\frac{l_0 + u}{l_0}\right) - \varepsilon^{mis}, \quad (1)$$

$$\varepsilon_a^{mech} = \ln\left(\frac{l_{0a} - u}{l_{0a}}\right) - \varepsilon_a^{mis}, \quad (2)$$

with l_0 and l_{0a} the initial length of specimen and actuator beam, respectively. Assuming that the actuator material, here Si_3N_4 , is elastic [25, 26] the stress is given by

$$\sigma_a = E_a \varepsilon_a^{mech}, \quad (3)$$

where E_a is the actuator modulus. The stress in the sample can be calculated using

$$\sigma = \sigma_a \frac{A_a}{A}, \quad (4)$$

where A_a and A are the actuator and test specimen cross-sectional area, respectively. Hence, the final equations to extract the true stress (σ) and true strain (ε^{mech}) in the specimen write

$$\begin{cases} \varepsilon^{mech} = \ln\left(\frac{l_0 + u}{l_0}\right) - \varepsilon^{mis} \\ \sigma = E_a \frac{S_a}{S} \left(\ln\left(\frac{l_{0a} - u}{l_{0a}}\right) - \varepsilon_a^{mis} \right) \end{cases} \quad (5)$$

In order to precisely determine the stress and the strain, the effect of the underetching and of the change of thickness along the width have been considered. The corrections are explained in Appendix.

2.1.3 Stability analysis

This section describes the relationship between the stiffness of one elementary test structure and the elastic and geometrical parameters. The objective is to compare our results with the analysis reported in Refs. [2, 29] in which a stability index was derived for the unstable propagation of an incipient shear band in metallic glasses. The stability of a loaded material specimen undergoing a localization process (e.g. shear band or diffuse necking) is affected by the elastic energy stored in the test machine and in the specimen, and hence related to their stiffness. A larger machine stiffness with respect to the sample stiffness lowers the amount of elastic energy distributed into the machine, thereby promoting a more stable response. The stability index, which correlates the ductility to the stiffness parameters and specimen dimensions, is defined as

$$L(1 + S), \quad (6)$$

where L is the length of the specimen and S is the ratio between the specimen stiffness (k_s) and machine stiffness (k_a), i.e.

$$S = \frac{k_s}{k_a}. \quad (7)$$

An advantage of the present lab-on-chip method compared with classical testing machines is that the stiffness of both the actuator and specimen is precisely known on the basis of the dimensions and elastic moduli:

$$k_a = E_a A_a / L_a, \text{ and } k_s = E_s A_s / L_s, \quad (8)$$

in which E , A , and L represent the elastic modulus, the cross sectional area and the length of the specimen and actuator, respectively. As a matter of fact, the actuator acts as a spring with a known stiffness.

2.2 Deposition and characterization of $Zr_{65}Ni_{35}$ TFMGs

The deposition by DC-magnetron sputtering of $Zr_{65}Ni_{35}$ (% at.) TFMGs has been explained in Refs. [21, 22, 30]. The composition has been checked by energy dispersive X-ray spectroscopy (EDS) and with electron probe micro analysis (EPMA) with no significant spatial variation [21, 22]. The elastic properties were extracted by Brillouin spectroscopy [22] giving $E = 72 \pm 2$ GPa and $\nu = 0.40 \pm 0.05$, while the amorphous structure was confirmed by X-ray diffraction (XRD) and transmission electron microscopy (TEM) [21, 22]. In the present study, aberration corrected HRTEM experiments have been carried out at 200 kV in a FEI Titan 80-300 “cubed” microscope in order to confirm the amorphous structure and to look for evidences of shear bands in the deformed specimens. Cross-sectional TEM thin foils were prepared from freestanding beams using the lift out method in a Helios FEI dual beam FIB/SEM. A protective platinum layer using electron beam assisted deposition has been used. The final thinning was performed using an of 2 kV/0.2 nA in order to minimize damage during high voltage FIB.

3. Results

3.1 Mechanical test results

Figure 2 shows the stress – strain curve for the 550 nm-thick specimens with different geometries, as reported in Table 1. As in the case of bulk specimens Refs. [2, 3], a purely elastic behavior with no or only very small amount of plastic deformation is observed. The maximum stress varies from 2200 ± 70 GPa for the 1 μm -wide specimens (Figure 2a) down to 1650 ± 70 GPa for the 4 μm -wide ones

(Figure 2c). The maximum deformation (ϵ) decreases from 3.1% down to 2.2%, while the elastic modulus (E) is constant and equal to 72 ± 5 GPa, in agreement with earlier Brillouin spectroscopy results performed on homogeneous thin film deposited on Si wafer [21, 22].

Figure 3 compares the true stress-true strain responses for the 360 nm-thick specimens involving different widths and lengths (see Table 1). The elastic modulus E is equal to 72 ± 5 GPa, again in agreement with earlier measurements [21, 22]. The yield strength is not affected by the length of the beam, while it varies with the width ranging from 2850 ± 80 MPa down to 1560 ± 80 MPa for 1 and 4 μm -wide beams, respectively. The ductility is very large, reaching a maximum of $14.5 \pm 0.1\%$ for the 25 μm -long and 1 μm -wide beam (Figure 2a). Note that rupture is reached only with the 1 μm -wide specimens. For the other widths, the deformation imposed by the longest actuator was not sufficient to reach fracture. However, a clear decrease of the fracture strain is observed when increasing specimen length from 25 μm up to 100 μm , as discussed later.

Figure 4 shows the true stress – true strain curve for a 200 nm-thick beams with different lengths and widths. As for 360 nm-thick specimens, the curves show good reproducibility on the elastic modulus (equal to 72 GPa) and on the yield strength, the last one being slightly affected by the beam length. The yield strength decreases from 3280 ± 80 MPa down to 1750 ± 80 MPa when the width of the beam increases from 1 to 4 μm . As for 360 nm-thick films, a large ductility is observed, reaching $15 \pm 0.1\%$ for 25 μm -long and 1 μm -wide specimen (Figure 3a).

A large ductility and yield strength is reported for the 110-nm thick specimens as well, see Figure 5. The curves show very good reproducibility with a very small scatter among the different lengths despite the very small dimensions. Note that the maximum yield strength (3300 ± 70 MPa) is obtained for the 25 μm -long and 2 μm -wide beam, while it decreases down to 2100 ± 70 MPa for a 4- μm wide beams. The maximum fracture strain is reached for the 25 μm long and 2 μm -wide beam being equal to

$11.8 \pm 0.1\%$. As for 360 and 200 nm-thick specimens the fracture strain depends on the beam length, showing the largest values for shorter beams. Note also that only the 2 μm -wide beams reach fracture.

3.2 SEM and HRTEM characterization

Figure 1c shows SEM micrographs of a specimen with dimensions 25 μm x 2 μm x 110 nm (black squares in Figure 5a) deformed by 11.8% with no evidence of shear band mediated localization. No shear band was ever observed by SEM on any of the specimens tested in this study. In order to further validate this observation, HRTEM characterizations have been carried out. Figure 6a is a micrograph obtained on a cross-sectional FIB thin foil prepared from a 360 nm-thick as-deposited film. Only a homogenous maze-like pattern typical of an amorphous structure can be observed. No crystal-like ordered regions with lattice fringes are detected. The selected area electron diffraction (SAED) pattern shown in the upper right of Figure 6a exhibits a full halo ring with no detectable diffraction spots. Cs corrected HRTEM images and SAED patterns taken in 360 nm-thick films deformed at 12% show similar observations, see Figure 6b. It is worth noting that the HRTEM observations covered all the FIB cross-sectional foils of the deformed films (i.e., more than 3000 HRTEM images have been acquired at the resolution shown in Fig. 6a,b). Therefore, no shear bands have been detected by SEM or by Cs corrected HRTEM in the deformed samples. This supports that the deformation is homogenous throughout the entire specimen in agreement with the large tensile plastic strains reached with most test geometries (except with the 550 nm-thick films) which would not be possible with the development of shear bands.

Figure 7 shows a SEM image of the fracture surface of a broken beam for a 360 nm-thick specimen. Specifically, it can be noted that the crack propagates in the width direction involving a mirror-like zone followed by corrugations. The morphology of the fracture surface is similar to the pattern observed in earlier studies on thin film metallic glass coatings in Refs. [21, 22, 31]. The origin of this failure pattern was explained by a geometrical confinement effect. Nevertheless, the corrugation pattern is much less

periodic here. Note that the orientation of the fracture surface is difficult to accurately determine. However, the ductile-like fracture surface supports the idea that the fracture surface should be inclined with an angle between 40 and 50° with respect to the normal to the plane, as for BMGs deformed in tension [3].

4. Discussion

A first important preliminary point regarding the discussion of the results presented above is the fact that the elastic modulus E is constant, independent on film thickness and width. This is one indication that all specimens tested in this study involve a similar atomic structure. This conclusion was already drawn in Refs. [21, 22] based on Brillouin spectroscopy results, giving the same constant value of elastic modulus independent on film thickness. Hence, the reasons for the size effects as determined with the on-chip tensile tests must, most probably, not be found in a change of the atomic structural arrangement and are thus not *intrinsic* size effects related to the changes of local order with the specimen dimensions. Another important aspect of these results is that each single point of the stress-strain curve corresponds to a single specimen and their good alignment on the tensile curve demonstrate the excellent reproducibility of the results.

a) Size effects on the yield strength

Figure 8a and 8b show the evolution of the yield strength (σ_y) as a function of the thickness and of the cross-sectional area (A), respectively. The yield strength has been taken as the 0.2% offset from the linear elastic behavior for thicknesses equal to 360, 200 and 110 nm. In the case of the 550 nm film thickness, the yield stress is taken as the maximum stress which is a reasonable approximation for most curves considering that they exhibit some minor amount of plastic deformation. Hence, specimens with similar

cross-sectional area involve similar σ_y independent on the smallest cross-section dimension, with no effect of the sample length out of the experimental scatter.

Figure 8a shows no obvious relationship between the yield strength (σ_y) – obtained using the data provided by the stress-strain curves in Figures 2 to 5 – and the thickness. The same data plotted as a function of the cross-sectional area (A) or the square root of the cross-sectional area (\sqrt{A}) exhibit a clear monotonic evolution (Figure 8b).

The σ_y for the largest specimen sizes, i.e. in the 550 and 360 nm-thick, 4 μm -wide specimens, is close to the one expected for the Zr-based BMGs (1600-1800 MPa) [3]. However, the behavior of the 360 nm-thick films is very different than in BMGs as it involves significant amount of plasticity after the onset of plastic yielding. This means that the onset of plasticity is not controlled by a shear banding process, as confirmed by electron microscopy. Furthermore, when the cross-section of the specimen decreases, a progressive increase of the yield stress is observed for cross-section area smaller than roughly 0.6 μm^2 . This increase is important since the maximum value obtained for cross-section area of around 0.2 μm^2 is nearly doubled. Note that a cross-section area A equal to 0.6 μm^2 corresponds to a circular section of a pillar with diameter equal to almost 1 μm and that these results agree with other studies on size effects of micro-scale metallic glass specimens loading either under compression [14, 15] or tensile conditions [7, 8]. This trend has been also reported by the Greer *et al.* [2], within Figure 53, summarizing the overall results carried out by many authors in the literature.

The model proposed by Johnson and Samwer [32] gives an upper bound estimate of the ideal yield stress as,

$$\gamma_y = \gamma_{C0} - \gamma_{C1}(T/T_g)^{2/3} \quad , \quad (9)$$

where γ_y and T_g are the elastic strain limit in shear and the glass transition temperature, respectively. T_g , equal to 421°C, has been estimated by measuring the electrical resistivity as a function of the temperature for $Zr_{65}Ni_{35}$ metallic glass films on a Si substrate. Ma and Cheng [33] validated equation (9) by setting the fitting parameters as $\gamma_{C0} = 0.11$ and $\gamma_{C1} = 0.09$. Since metallic glasses are isotropic, equation (9) can be converted to obtain the ideal strength limit (σ_y) in uniaxial tension using $\sigma_y = \varepsilon_y / E = \gamma_y / E(1 + \nu)$ in which ν and E are the Poisson ratio and the elastic modulus, respectively. With this approximation, the calculated ideal yield strength would be around 3200 MPa. This value is represented by a band in Figs. 8a and b, which matches very well with values obtained by the specimens exhibiting for smallest cross-sectional area.

This analysis shows that the yield stress evolution with the cross-sectional area can be divided into three domains, as also reported by Greer *et al.* [2]. Region 3 corresponds to cross-section areas larger than $\sim 0.6 \mu\text{m}^2$ where the yield stress is independent on the section and roughly equal to the one expected for BMG, Refs. [2, 3]. Region 2 lying between $\sim 0.30 \mu\text{m}^2$ and $\sim 0.6 \mu\text{m}^2$ corresponds to the cross-section range where σ_y increases when reducing the cross-section area. Finally, since the ideal yield stress is reached for the smaller specimen sections, another behavior is expected for cross-section area below $\sim 0.30 \mu\text{m}^2$.

This “three-regime” scenario agrees with the explanation proposed by Greer *et al.* [2]. In their review, the authors differentiate between two nucleation regimes for the shear banding process, the nucleation stress being equal to the yield stress, which sets the onset of plastic deformation. It is important at this point to make the difference between the nucleation mechanism and the final existence of a mature (and visible) shear band. The article of Shimizu *et al.* [4] shows – using molecular dynamics simulations – that the shear band nucleation phenomenon can be stable until a critical length without leading to catastrophic propagation throughout the sample. Greer *et al.* [2] demonstrate that, in the case of bulk

samples, the nucleation of a shear band is heterogeneous and certainly linked to the existence of flaw defects (casting or surface imperfection) with a size greater than a critical flaw size that would be around ten Shear Transformation Zone (STZ) diameters, roughly corresponding to 10 nm. In that case, the yield stress is independent on the sample size. This zone corresponds to what they called “regime C” in their Figure 52. When the sample size is reduced, flaw defects become statistically smaller than this critical size and the shear band nucleation mechanism becomes at least partially homogeneous. In that case, the yield stress is directly linked to the probability to activate a sufficient number of fertile STZs in a shear plane and will hence be size dependent and certainly “cross-section dependent” as observed in the present study, see Figure 8b. This transition regime is called “B” in their work and corresponds to the “regime 2” in Figure 8b. Moreover, the authors hypothesize that the yield strength would reach values close to the ideal yield strength as measured in the present work for the smallest cross-sectional areas. Finally, at a point, the strength would decrease for even smaller sizes as a result of surface diffusion controlled atomic mobility. They called this last regime “A” which would correspond to the left part of “regime 1” for which no experimental data have been obtained in this study.

The present results are in accordance with the description of Greer *et al.* [2] regarding, at least, the magnitude of the yield stress corresponding to the onset of plastic deformation. However, in “regime 1” and “2” corresponding to homogeneous nucleation, it is not clear why the yield stress should increase when the cross-sectional area is decreasing. The present results suggest that, in such films, plasticity develops homogeneously through atomic rearrangements, most probably through the activation of STZs, which do not develop, through mutual interaction, into mature shear bands due to the small dimensions [2, 8, 34, 35]. The picture which emerges from our experimental data is that, in order to produce overall plasticity inside the specimen, there is a need, as for polycrystals, for the plastic events to collectively percolate throughout the entire sample. In polycrystals, the regime of microplasticity in which some dislocations activity develops in some specific grains does not lead to macroplasticity [8, 36]. It is only

when there is full percolation throughout a vast number of grains of a dislocation driven mechanism that macroplasticity starts [8, 36]. In analogy, the spread of plastic deformation in the entire gauge length of the metallic glass specimens is allowed when cooperative motion or activation of STZ occurs in every sub-volume of each small sections of the specimens. Our results show that cooperative activation of STZ operations is made more and more complex as the size is reduced (in agreement with Ref. [35]), probably because of the decreasing probability to find fertile regions for STZ transformation in every sub-sections of the specimens with decreasing the size.

b) Plastic deformation and failure mechanics

Figure 9 shows the variation of the fracture strain as a function of the stability index quantified by $L(I+S)$, where L is the specimen length and S the actuator-specimen stiffness ratio (k/k_{act}), see Ref. [2] and Section 2.1.3. Large ductility up to 15% is attained for small $L(I+S)$ and thus small k/k_{act} , indicating a stabilizing effect associated to stiff actuators, as reported in the literature for BMGs under compressive stress Refs. [2, 29] and for *in-situ* TEM tensile tests Ref. [10].

The fracture of $Zr_{65}Ni_{35}$ films involves thus a cooperation or competition between two aspects. Larger specimens have a higher probability of containing larger imperfections or defects from which fracture can be initiated. Now, the stability of the incipient fracture process depends on the stiffness of the machine which imposes the loading, as quantified by $L(I+S)$. Considering that fracture is initiated by a plastic localization process, it is well known that, indeed, the ductility heavily depends on the magnitude of the largest imperfection as well as on the overall amount of elastic energy stored in the system, see Ref. [36] for a recent theoretical analysis of plastic localization in thin films. These elements can be used to explain the variation of the fracture strain summarized in Figure 9 through answering three questions.

1. Why is plastic deformation homogeneous with no early localization (necking or shear bands)?

It was explained above that the origin of the evolution of the yield stress with cross-section area comes from the geometrical constraint put on the collective and cooperative activation of STZ through long range correlations. This means that, inherently, the onset of plasticity is not connected to a phenomenon involving a tendency to produce mature shear bands at the early stages of deformation. This is also favored by the homogeneity of the film material produced by vapor phase deposition, which avoids the presence of stress concentration and allows the plastic deformation to initiate in the entire gauge section within a small range of applied deformation. But this does not explain why, after the onset of plasticity, the deformation remains homogenous. Indeed, the absence of strain hardening should, in principle, lead to a tendency for plastic localization soon after the onset of plasticity.

The reason which explains the homogenous deformation observed in the present thin films is their relatively high strain rate sensitivity (m). In Ref. [22], it was indeed shown, based on nanoindentation experiments, that the rate sensitivity exponent of $Zr_{65}Ni_{35}$ thin metallic glass films m is equal to ~ 0.03 . This is a high value for metallic glasses [22]. Rate sensitivity plays the same role as strain hardening in retarding plastic localization and in allowing homogenous deformation such as for instance in metallic polycrystals when deformed at high temperature. The localization analysis performed in Ref. [36] – following the pioneering works for instance by Hutchinson and Neale [37] – show that, for such value of m , and a low strain hardening exponent, a ductility between 10 and 20% can be attained. This means that a material with $m \sim 0.03$ is potentially capable of maintaining the deformation homogenous up to a strain of more than 10%, in agreement with the results for the films with thickness below 360 nm. Further TEM analyses have to be performed to find the physical root cause for the high rate sensitivity, hence for the high capacity for thermal activation of STZs process, by looking at the atomic arrangement of the present metallic glass films.

2. How can we explain the high fracture strain in films with thickness ≤ 360 nm?

It is not because a material has a high rate sensitivity (and/or a high strain hardening capacity) and the intrinsic capacity to resist plastic localization that a test specimen or structural element will exhibit large fracture strain. Extrinsic aspects can play a role as well. As expected above, the first element is that the stability of the deformation is partly dictated by the amount of elastic energy that is stored and which can be potentially released in the test structure upon localization. Figure 9 has indeed shown that the stability index $L(1+S)$ provides a clear rationale to explain the variation of the fracture strain in the films with thickness equal or below 360 nm. The second element is the presence of imperfections. Imperfections play a major role on setting the resistance to plastic localization, see e.g. [36]. For instance, a local reduction of the cross-section area by 2% compared with the rest of the specimen, can lead to a reduction of the ductility by one half. The high fracture strain attained in the films with thickness below 360 nm necessarily means that the films exhibit very limited imperfections.

3. How can we explain the difference in fracture behavior between the 550 nm-thick films and the others?

The 550 nm-thick films, while following the trend of the other thicknesses regarding the yield stress, in terms of yield strength variation versus cross-section area, show a much lower fracture strain typical of BMG. On the other hand, the widest 360 and 200 nm-thick films exhibit a strength level in the range of BMG (regime 3 in Fig. 8) while maintaining a high ductility above 8%. This marked difference in the behavior clearly proves the disconnect between the mechanisms dictating the onset of plasticity and the fracture mechanism in the present films, as we explained in the answer to question 1.

The fact that the fracture stress of the 550 nm-thick films varies with the width means that a fracture mechanics criterion based on a brittle failure mechanism should be discarded because such a mechanism should lead to the same fracture stress. As a matter of fact, the occurrence of fracture in the 550 nm-thick

films requires that the plasticity mechanisms have started to proceed at least just before (otherwise these films would not follow the trend in Fig. 8). Moreover, considering that the 550 nm films exhibit the same elasto-viscoplastic response as the other films thicknesses, with rate sensitivity $m \sim 0.03$ (see Ref. [22]), we should expect the same high level of ductility. In order to explain the much lower fracture strain one possibility involves the presence of larger imperfection sizes compared with the other films thicknesses, accelerating the initiation of the failure process, in agreement with the explanations given to question 2. In addition, there is an effect of the smallest length associated to the cross-section (i.e. the thickness) not on the initiation of plasticity, but on the activation of the shear banding process. As explained by Shimizu *et al.* [4] there is a length below which the shear banding process is impeded. If a shear band can form and propagate over a length larger than a critical value, the propagation can become catastrophic and ultimately lead to fracture. This would mean that for the 550 nm-thick film, the failure does not depend anymore on the cross-section area but depends on the smallest dimension, which is the thickness.

In summary, the elements needed for a high ductility are either *extrinsic* (i) to avoid catastrophic shear banding by a homogenous plasticity process as constrained here by the small size, (ii) to increase the loading device stiffness, (iii) to minimize the presence of imperfections, and *intrinsic* (iv) to favor high rate sensitivity or to increase strain hardening capacity as proposed in recent papers of Hufnagel *et al.* [38]. In this work, the low (> 550 nm) or high (< 360 nm) ductility is the result of a competition between the four elements in which the *intrinsic* atomic structure plays a role in dictating the threshold for the activation of STZs, the likelihood to generate mature shear bands for a fixed set of specimen stiffness and geometry, and the strain rate sensitivity.

5. Conclusions

A vast amount of tensile tests performed on-chip of thin ZrNi metallic glass films combined with TEM characterization lead to the following set of conclusions:

- The yield stress increases with decreasing specimen size up to the ideal yield strength. This size effect is related to the specimen cross-sectional area and not to the smallest dimension of the section;
- HRTEM demonstrates the absence of shear bands indicating homogenous deformation. The homogenous deformation is interpreted as being the result of the correlated activation of STZs throughout the volume of the specimen without triggering any catastrophic shear bands owing to the geometry constraint;
- The films with thicknesses below 360 nm exhibit unexpectedly large fracture strain in tension, reaching 15%. This ductility is shown to depend on the stiffness of the elementary test structure through a simple stability index. The high ductility values most presumably results from a high rate sensitivity exponent combined to limited amount of imperfections. The thicker films (550 nm) exhibit much lower ductility in agreement with the values typically found for bulk metallic glasses;
- There is a disconnect, in the $Zr_{65}Ni_{35}$ thin films, between the mechanisms leading to the onset of plasticity and the failure mechanisms, while in BMGs they are both related to the shear banding process.

Further efforts will aim at explaining the physical origin of the relatively high rate sensitivity through unravelling the elementary deformation mechanisms using nanobeam electron diffraction as well as *in-situ* TEM nanomechanical testing. These techniques will be used to investigate the evolution of the local order in the thin ZrNi metallic glass films with increasing deformation.

Acknowledgments

This work has been funded by the Belgian Science Policy through the IAP 7/21 project. We acknowledge IDS-FunMat for the PhD financial support. We thank the Renatech network and the PTA (Plateforme Technologique Amont) in Grenoble (France) for TFMG deposition facilities. The WINFAB infrastructure at the UCL and the help of R. Vayrette and M. Coulombier for the on-chip tests. H. Idrissi is currently mandated by the Belgian National Fund for Scientific Research (FSR-FNRS).

Appendix. Extraction of mechanical properties: detailed analysis considering corrections for underetching, dogbone geometry, and thickness variation

In order to precisely determine the stress and strain, the underetching and the variation of the specimens thickness along the width must be taken into account. The underetching leads to an effective beam length longer than the nominal value. This effect – estimated by the size of brighter zones at the bottom and lateral edges of test structures – amounts to $\sim 20 \mu\text{m}$ (Figure A1).

On the other hand, a thickness variation of the specimen is induced by the lithography lift-off process as a results of the shadow effect due to the photoresist during the sputter deposition. Figure 7 is a SEM image of a broken specimen showing the thickness variation along the width. Specifically, the thickness varies along the cross-section from 360 nm (left part in Fig. 7) down to 230 nm (right part of Fig. 7). The thickness variation has been systematically quantified for all specimens and the procedure below has been used to calculate precise stress-strain values.

a) Accurate extraction of displacement change corresponding to the contraction of the actuator beam

First, the actuator length (l_a) is given by

$$l_a = l_a^{nom} + l_{ue}, \quad (A1)$$

where l_a^{nom} is the nominal length of the actuator and l_{ue} is the underetching length equal to $\sim 20 \mu\text{m}$.

Second, the measured displacement (u_{meas}) is the sum of the contraction of the actuator length (u_a) plus a displacement related to the underetch zone contraction (u_u):

$$u_{meas} = u_a + u_u, \quad (A2)$$

in which u_u can be estimated as

$$u_u = -\varepsilon_a^{mis} l_{ue}, \quad (A3)$$

where ε_a^{mis} is the actuator mismatch equal to -0.0030. Hence, by the exact actuator change of length (u_a) can be found by combining equations (A2) and (A3) and setting the underetching length equal to the measured bright zone (Figure A1).

b) Determination of the true displacement imposed to the gauge section of the specimen

The measured displacement (u_{meas}) can be written as, see Ref. [26],

$$u_{meas} = u + u_{db} + u_u, \quad (A4)$$

where u is the real displacement, u_{db} is the displacement of the dogbone part (namely the zone with the width reduction) and u_u is the underetching displacement corresponding to the specimen side. According to Ref. [27], u_{db} and u_u can be estimated as

$$u_{db} = u_{meas} (w / w_{db}^{eff}) (l_{db} / l_{tot}), \quad (A5)$$

$$u_u = u_{meas} (w / w_u^{eff}) (l_u / l_{tot}), \quad (A6)$$

where w , w_{db}^{eff} , and w_u^{eff} are, respectively, the width of the specimen, the effective width of the dogbone and the effective width of the underetching, while l_{db} , and l_{tot} represent the length of the dogbone and of the entire specimen ($l_{tot} = l + l_{db} + l_u$), respectively.

According to Ref. [27], equation A6 can be simplified, to extract the real displacement (u) avoiding a direct estimation of w_{db}^{eff} and w_u^{eff} as

$$u = u_{meas} - u_{meas} \alpha (l_{db} + l_u) / l_{tot}, \quad (A7)$$

with

$$\alpha = w / w^{eff}, \quad (A8)$$

where w^{eff} is the effective width of the specimen. In this study, α is taken equal to 0.3 as in Ref. [27]. Hence, after this step u can be calculated for all loaded structures under elastic loading. For structures at larger strains, the correction of the last elastic specimen is used, because the dogbone part and the underetching regions will involve almost no changes of deformation as the stress is almost constant owing to the almost perfectly plastic behavior (see Section 1.3).

c) True strain in the specimen

The mechanical strain (ε) in the specimen can be calculated as

$$\varepsilon = \ln\left(\frac{l+u}{l}\right) - \varepsilon^{mis}, \quad (A9)$$

where ε^{mis} is equal to +0.0017.

d) True stress in the specimen

The stress (σ) can be calculated as

$$\sigma = K \left(\ln \left(\frac{l_a - u}{l_a} \right) - \varepsilon_a^{mis} \right), \quad (\text{A10})$$

where ε_a^{mis} is the actuator mismatch equal to -0.0030, while K can be written as

$$K = \frac{E_a w_a t_a}{\beta w t}, \quad (\text{A11})$$

where t_a and t are the thickness of the actuator and specimen, respectively, while β is an adimensional parameter which quantifies the effective change of the beam thickness given by $\langle t_{real} \rangle / t_{nominal}$; here, β usually ranges in between 0.6 and 0.7 depending on the specimen series.

References

- [1] Ashby M, Greer A. Metallic glasses as structural materials. *Scr Mater* 2006;54:321-6.
- [2] Greer AL, Cheng YQ, Ma E. Shear bands in metallic glasses. *Mater Sci Eng, R* 2013;74:71-132.
- [3] Schuh CA, Hufnagel TC, Ramamurty U. Mechanical behavior of amorphous alloys. *Acta Mater* 2007;55:4067-109.
- [4] Shimizu F, Ogata S, Li J. Yield point of metallic glass. *Acta Mater* 2006;54:4293-8.
- [5] Cao AJ, Cheng YQ, Ma E. Structural processes that initiate shear localization in metallic glass. *Acta Mater* 2009;57:5146-55.
- [6] Volkert CA, Donohue A, Spaepen F. Effect of sample size on deformation in amorphous metals. *J Appl Phys* 2008;103:083539.
- [7] Jang D, Greer JR. Transition from a strong-yet-brittle to a stronger-and-ductile state by size reduction of metallic glasses. *Nature Mater* 2010;9:215-9.
- [8] Greer JR, De Hosson JTM. Plasticity in small-sized metallic systems: Intrinsic versus extrinsic size effect. *Prog Mater Sci* 2011;56:654-724.

- [9] Chen CQ, Pei YT, Kuzmin O, Zhang ZF, Ma E, De Hosson JTM. Intrinsic size effects in the mechanical response of taper-free nanopillars of metallic glass. *Phys Rev B: Condens Matter* 2011;83:180201(R).
- [10] Deng Q, Cheng Y, Yue Y, Zhang L, Zhang Z, Han X, et al. Uniform tensile elongation in framed submicron metallic glass specimen in the limit of suppressed shear banding. *Acta Mater* 2011;59:6511-8.
- [11] Guo H, Yan PF, Wang YB, Tan J, Zhang ZF, Sui ML, et al. Tensile ductility and necking of metallic glass. *Nat Mater* 2007;6:735-9.
- [12] Tonnie D, Maass R, Volkert CA. Room temperature homogeneous ductility of micrometer-sized metallic glass. *Adv Mater* 2014;26:5715-21.
- [13] Chen DZ, Gu XW, An Q, Goddard WA, Greer JR. Ductility and work hardening in nano-sized metallic glasses. *Appl Phys Lett* 2015;106:061903.
- [14] Lee CJ, Huang JC, Nieh TG. Sample size effect and microcompression of $Mg_{65}Cu_{25}Gd_{10}$ metallic glass. *Appl Phys Lett* 2007;91:161913.
- [15] Lai YH, Lee CJ, Cheng YT, Chou HS, Chen HM, Du XH, et al. Bulk and microscale compressive behavior of a Zr-based metallic glass. *Scr Mater* 2008;58:890-3.
- [16] Kuzmin OV, Pei YT, Chen CQ, De Hosson JTM. Intrinsic and extrinsic size effects in the deformation of metallic glass nanopillars. *Acta Mater* 2012;60:889-98.
- [17] Chen CQ, Pei YT, De Hosson JTM. Effects of size on the mechanical response of metallic glasses investigated through in situ TEM bending and compression experiments. *Acta Mater* 2010;58:189-200.
- [18] Dubach A, Raghavan R, Loffler J, Michler J, Ramamurty U. Micropillar compression studies on a bulk metallic glass in different structural states. *Scr Mater* 2009;60:567-70.
- [19] Jiang QK, Liu P, Cao QP, Wang C, Li XL, Gao XY, et al. The effect of size on the elastic strain limit in $Ni_{60}Nb_{40}$ glassy films. *Acta Mater* 2013;61:4689-95.

- [20] Tian L, Cheng YQ, Shan ZW, Li J, Wang CC, Han XD, et al. Approaching the ideal elastic limit of metallic glasses. *Nat Commun* 2012;3:609:1-6.
- [21] Ghidelli M, Gravier S, Blandin J-J, Raskin J-P, Lani F, Pardoën T. Size-dependent failure mechanisms in ZrNi thin metallic glass films. *Scr Mater* 2014;89:9-12.
- [22] Ghidelli M, S. Gravier, J.-J. Blandin, P. Djemia, F. Mompiou, G. Abadias, et al. Extrinsic mechanical size effects in thin ZrNi metallic glass films. *Acta Mater* 2015;90:232-41.
- [23] Liu YH, Zhao F, Li YL, Chen MW. Deformation behavior of metallic glass thin films. *J Appl Phys* 2012;112:063504.
- [24] Zhang Q, Li Q-K, Li M. Processing dependence of mechanical properties of metallic glass nanowires. *Appl Phys Lett* 2015;106:071905.
- [25] Coulombier M, Guisbiers G, Colla MS, Vayrette R, Raskin JP, Pardoën T. On-chip stress relaxation testing method for freestanding thin film materials. *Rev Sci Instrum* 2012;83:105004.
- [26] Gravier S, Coulombier M, Safi A, André N, Boé A, Raskin J-P, et al. New on-chip nanomechanical testing laboratory-applications to aluminum and polysilicon thin films. *J Microelectromech Syst* 2009;18:555-69.
- [27] Vayrette R, Raskin J-P, Pardoën T. On-chip fracture testing of freestanding nanoscale materials. *Eng Fract Mech* 2015;150:222-38.
- [28] Boé A, Safi A, Coulombier M, Pardoën T, Raskin JP. Internal stress relaxation based method for elastic stiffness characterization of very thin films. *Thin Solid Films* 2009;518:260-4.
- [29] Han Z, Wu WF, Li Y, Wei YJ, Gao HJ. An instability index of shear band for plasticity in metallic glasses. *Acta Mater* 2009;57:1367-72.
- [30] Ghidelli M, Gravier S, Blandin J-J, Pardoën T, Raskin J-P, Mompiou F. Compositional-induced structural change in Zr_xNi_{100-x} thin film metallic glasses. *J Alloys Compd* 2014;615:S348-S51.

- [31] Ghidelli M, Volland A, Blandin J-J, Pardoën T, Raskin J-P, Momprou F, et al. Exploring the mechanical size effects in Zr₆₅Ni₃₅ thin film metallic glasses. *J Alloys Compd* 2014;615:S90-S2.
- [32] Johnson WL, Samwer K. A universal criterion for plastic yielding of metallic glasses with a $(T/T_g)^{2/3}$ temperature dependence. *Phys Rev Lett* 2005;95:195501.
- [33] Cheng YQ, Ma E. Intrinsic shear strength of metallic glass. *Acta Mater* 2011;59:1800-7.
- [34] Zhang Y, Mendeleev MI, Wang CZ, Ott R, Zhang F, Besser MF, et al. Impact of deformation on the atomic structures and dynamics of a Cu-Zr metallic glass: A molecular dynamics study. *Phys Rev B: Condens Matter* 2014;90.
- [35] Zhao P, Li J, Wang Y. Extended defects, ideal strength and actual strengths of finite-sized metallic glasses. *Acta Mater* 2014;73:149-66.
- [36] Pardoën T. Size and rate dependent necking in thin metallic films. *J Mech Phys Solids* 2014;62:81-98.
- [37] Hutchinson J, Neale K. Sheet necking-II. Time-independent behavior. *Mechanics of sheet metal forming*: Springer; 1978. p. 127-53.
- [38] Hufnagel TC, Schuh CA, Falk ML. Deformation of metallic glasses: Recent developments in theory, simulations, and experiments. *Acta Mater* 2016;109:375-93.

Table 1 | Dimensions of the specimen beams

Specimen thickness (nm)	Specimen width (μm)	Specimen length (μm)
110	2-4	25-50-100
200	1-2-4	25-50-100
360	1-2-4	25-50-100
550	1-2-4	25-50-100

List of Figures

Fig. 1. *The lab-on-chip method used to determine the stress-strain response; (a,b), schematic of the lab-on-chip before and after release. (c), SEM image of a deformed 25 μm x 2 μm x 110 nm freestanding specimen.*

Fig. 2. *True stress - true strain curves of 550 nm-thick specimens with different widths equal to 1, 2 and 4 μm , respectively (a), (b) and (c), and different lengths of 25, 50 and 100 μm .*

Fig. 3. *True stress - true strain curves of 360 nm-thick specimens with different widths equal to 1, 2 and 4 μm , respectively (a), (b) and (c), and different lengths of 25, 50 and 100 μm .*

Fig. 4. *True stress - true strain curves of 200 nm-thick specimens with different widths equal to 1, 2 and 4 μm , respectively (a), (b) and (c), and different lengths of 25, 50 and 100 μm .*

Fig. 5. *True stress - true strain curves of 110 nm-thick specimens with different widths equal to 2 and 4 μm , respectively (a) and (b), and different lengths of 25, 50 and 100 μm .*

Fig. 6. *Cs corrected HRTEM image on (a) as-deposited and (b) 12% deformed $\text{Zr}_{65}\text{Ni}_{35}$ TFMGs. SAED patterns obtained with a ~ 700 nm selected area aperture are shown in the upper right insets. A fully amorphous structure is observed before and after deformation. Shear bands have not been detected in the deformed films.*

Fig. 7. Fracture surface of a beam with a thickness equal to 360 nm, showing a mirror-like surface followed by corrugations.

Fig. 8. (a) Variation of the yield strength as a function of the thickness; (b) variation of the yield strength as a function of the cross-sectional area and of the square root of the cross-sectional. An assumed variation of the data (eye guide) is reported and the three deformation regimes are highlighted.

Fig. 9. Variation of the fracture strain as a function of $L(1+S)$, where S is the stiffness ratio k/k_{act} . The continuous line is guide for eyes.

Fig. A1. SEM micrograph of a lab-on-chip highlighting the underetching corresponding to the size of the brighter zones as indicated by horizontal and vertical arrows.

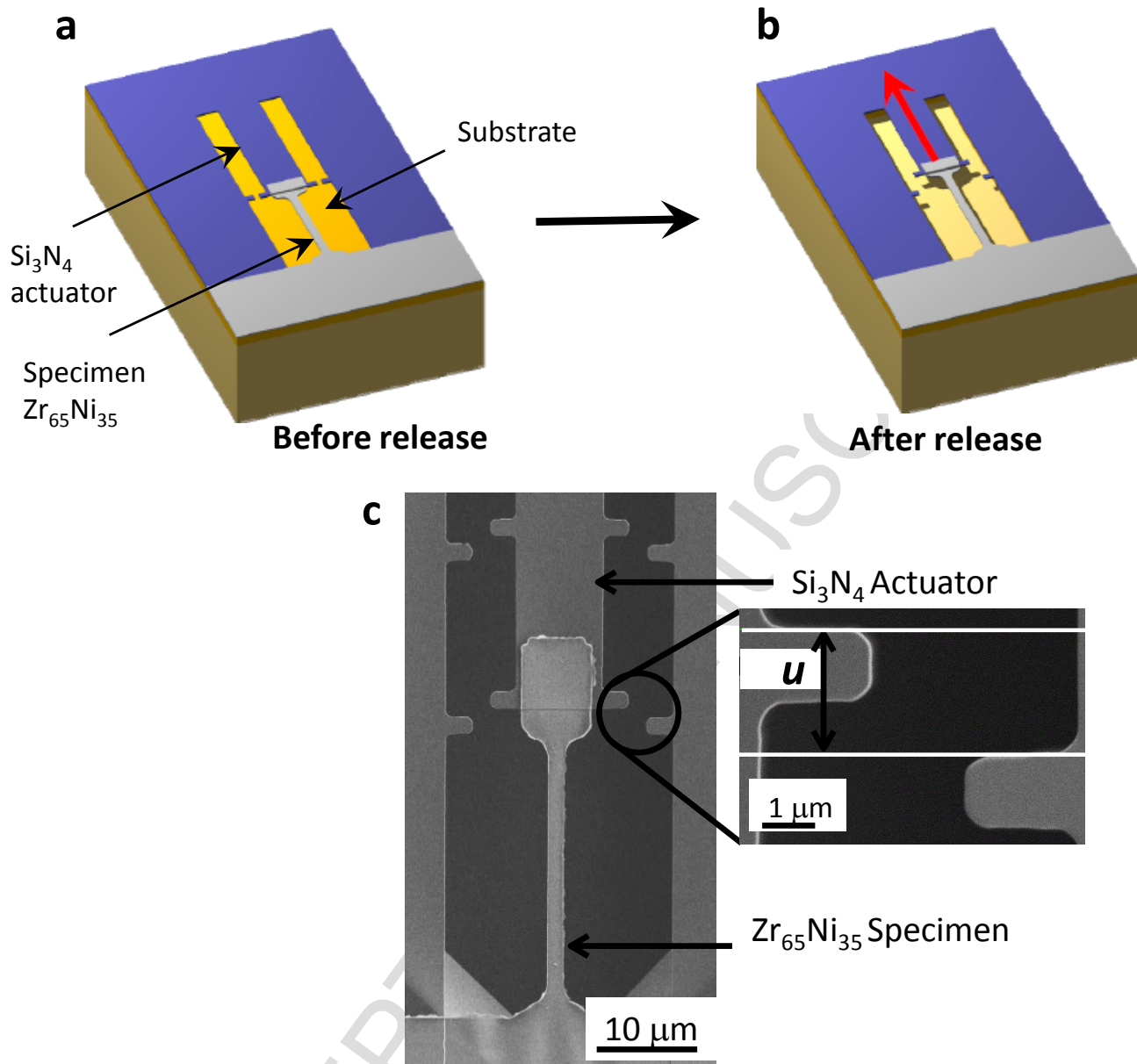


Figure 1

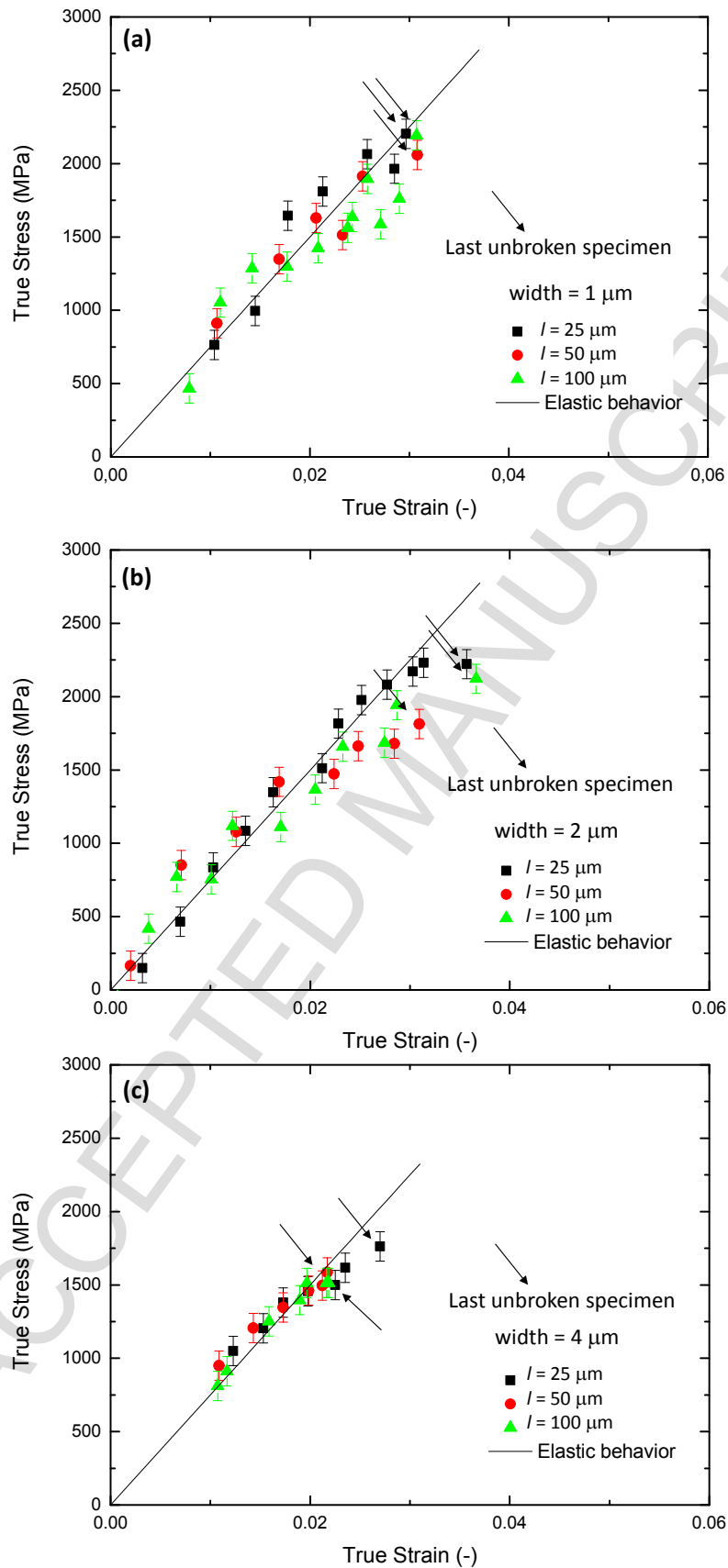


Figure 2

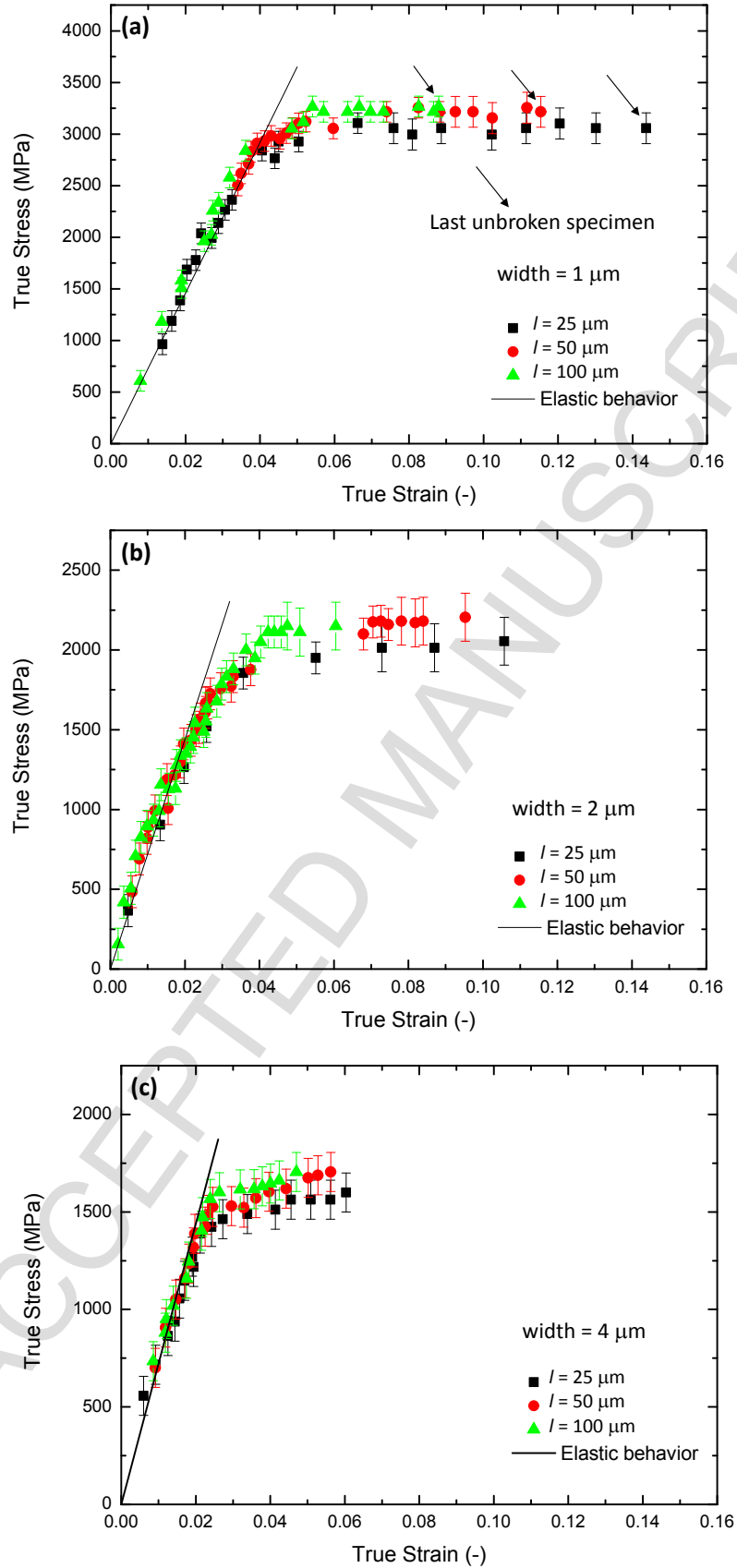


Figure 3

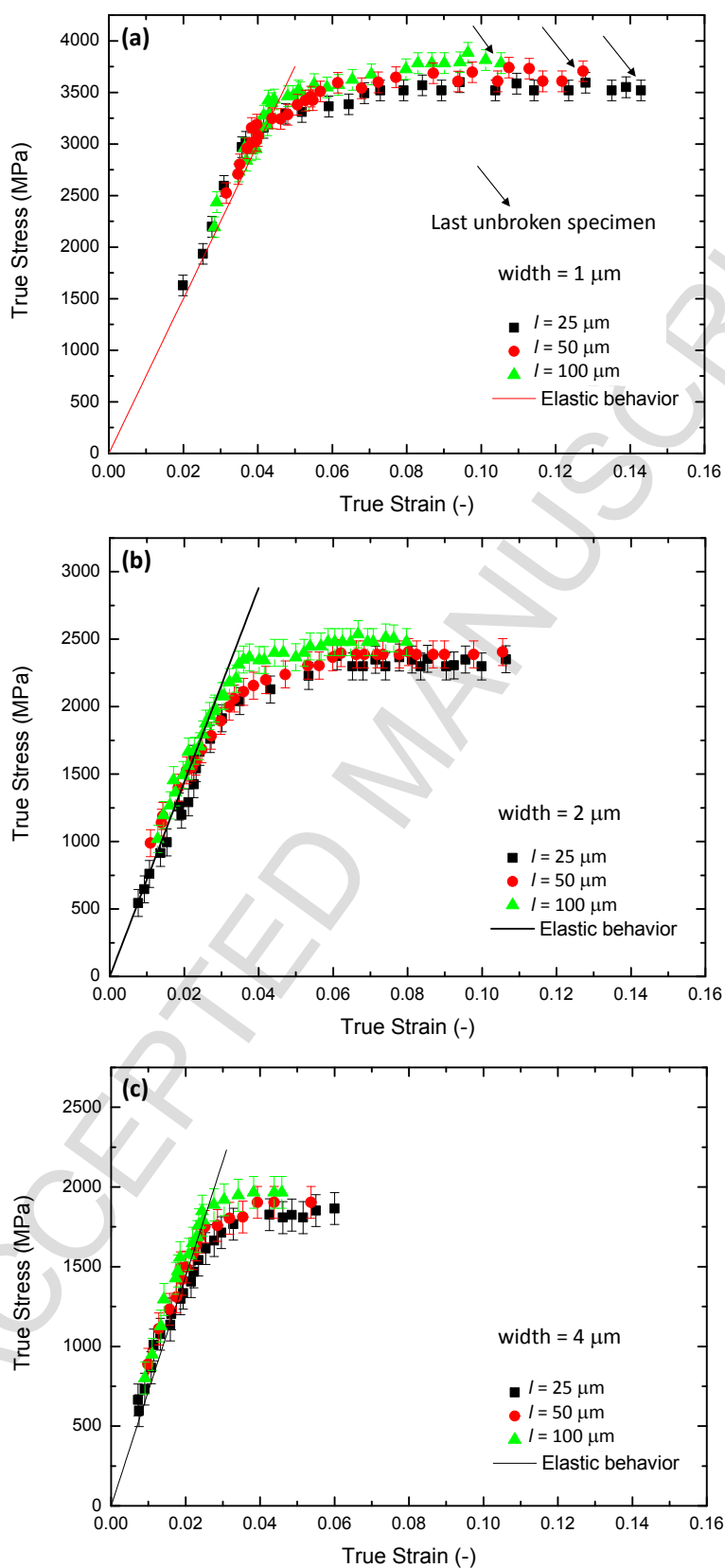


Figure 4

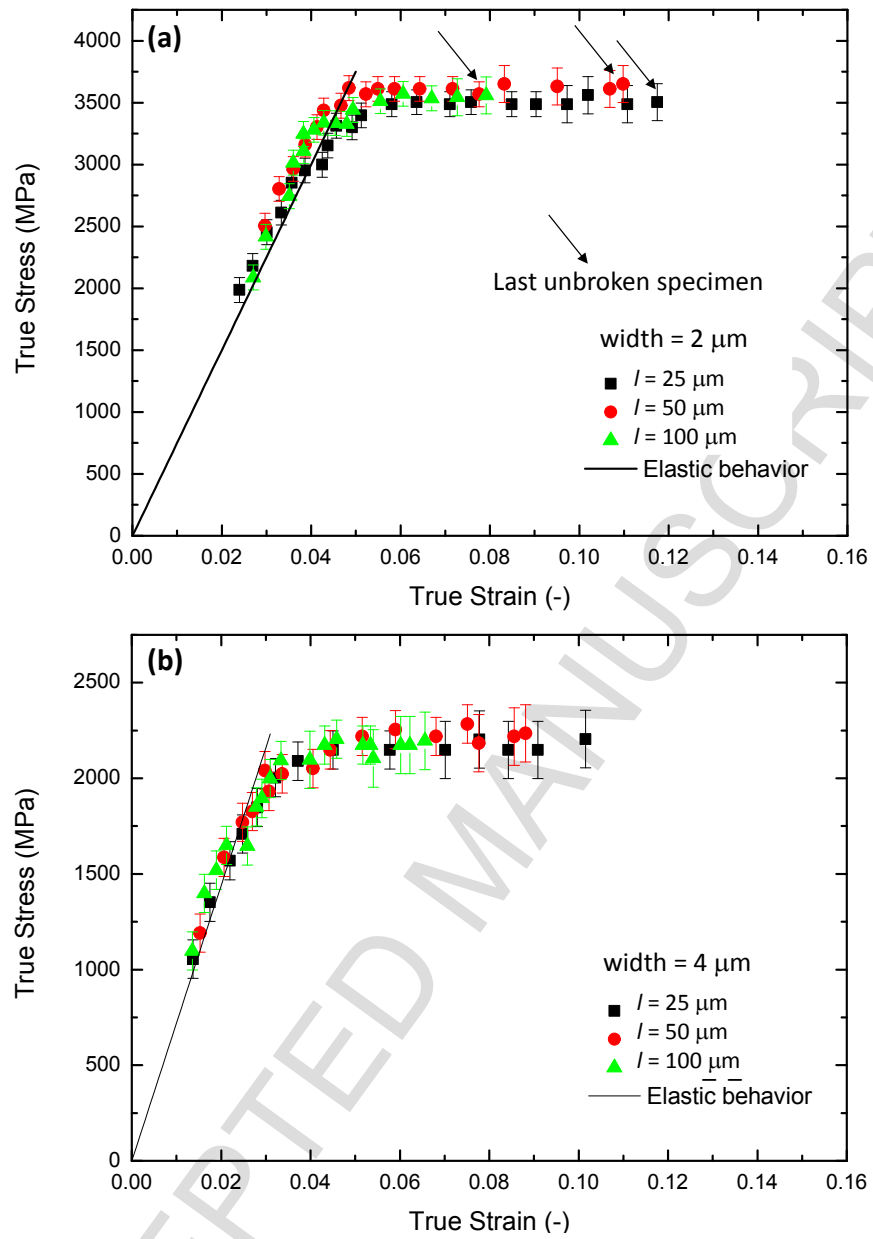


Figure 5

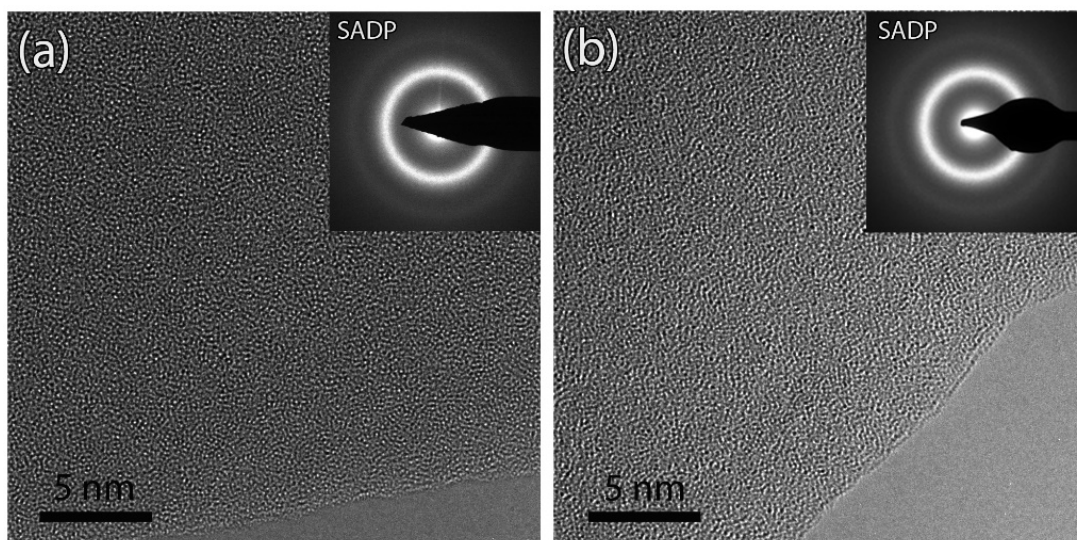


Figure 6

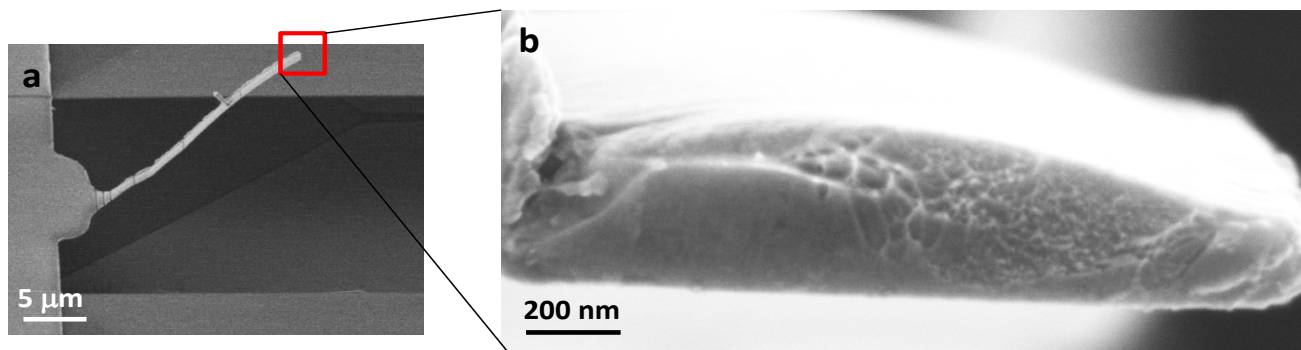


Figure 7

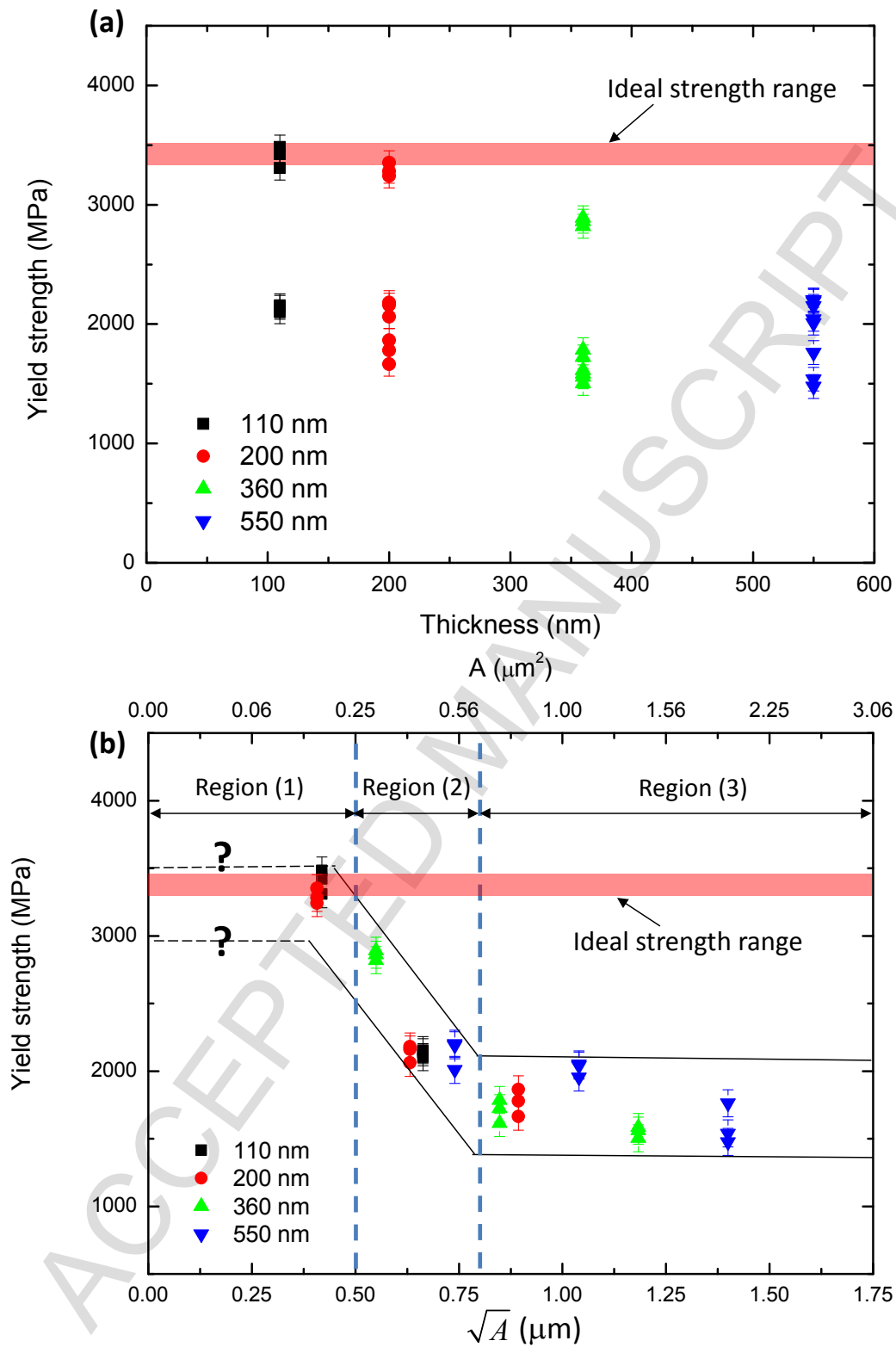


Figure 8

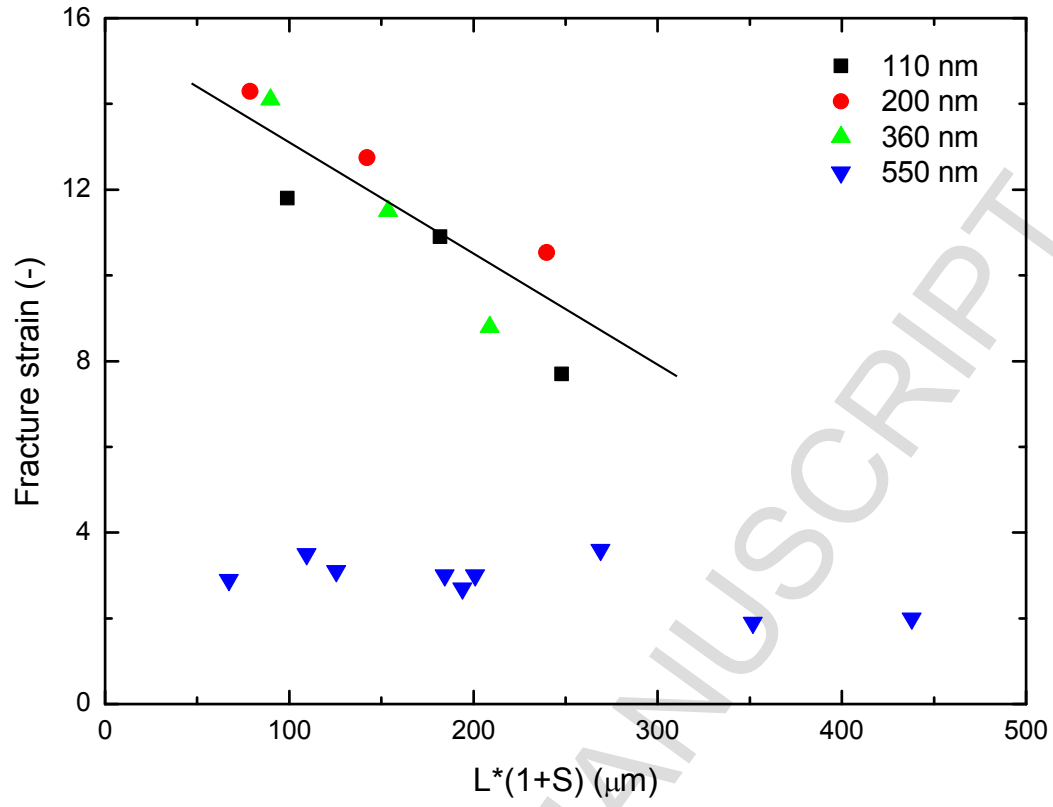


Figure 9

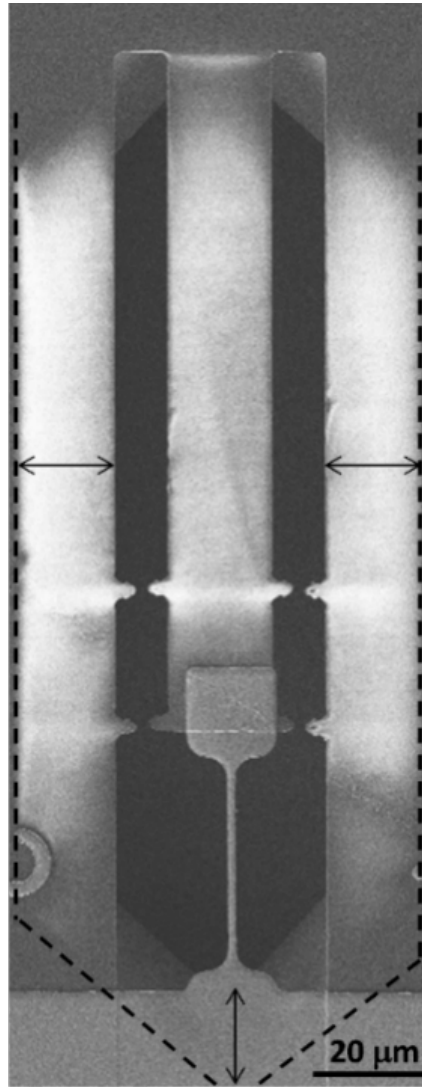


Figure A1